SCIENCE CHINA
Information Sciences

• RESEARCH PAPER •

January 2022, Vol. 65 112305:1–112305:12
https://doi.org/10.1007/s11432-020-2915-2

Collaborative representation with background purification and saliency weight for hyperspectral anomaly detection

Zengfu HOU[1], Wei LI[1*], Ran TAO[1], Pengge MA[2] & Weihua SHI[3]

[1]*School of Information and Electronics, Beijing Institute of Technology, Beijing* 100081*, China;*
[2]*School of Intelligent Engineering, Zhengzhou University of Aeronautics, Zhengzhou* 450015*, China;*
[3]*Urban-Rural Planning Administration Center, Ministry of Housing and Urban-Rural Development of the People's Republic of China, Beijing* 100081*, China*

Received 7 March 2020/Revised 4 April 2020/Accepted 12 May 2020/Published online 23 December 2021

Abstract Collaborative representation-based detection (CRD) has been developed in hyperspectral anomaly detection tasks and testified to be very effective; however, heterogeneous pixels in the background may affect the accuracy of linear representation and make its performance suboptimal. To address this issue, a background purification framework based on linear representation is proposed, in which an automatic outlier removal strategy based on initial coefficients is designed to purify the background. In the proposed method, the classic least squares technique is firstly adopted to obtain preliminary linear representation coefficients, which are positively correlated with its contribution to a central testing pixel. Then, using statistical analysis of the representation coefficients, purified background pixels are obtained. Furthermore, a saliency weight is applied to fully utilize the spatial information of inner window pixels. Extensive experiments with three real hyperspectral datasets show that the proposed method outperforms state-of-the-art CRD and other traditional detectors.

Keywords hyperspectral, anomaly detection, background purification, collaborative representation, saliency weight

Citation Hou Z F, Li W, Tao R, et al. Collaborative representation with background purification and saliency weight for hyperspectral anomaly detection. Sci China Inf Sci, 2022, 65(1): 112305, https://doi.org/10.1007/s11432-020-2915-2

1 Introduction

Different from traditional multispectral or panchromatic images, hyperspectral images (HSI) contain rich spectral information with a large number of bands and high spectral resolution [1–3]. These distinctive features provide unique advantages for target detection. And it has shown great potential applications in remote sensing ground observation, food safety, medical diagnosis, etc. In reality, prior knowledge of target spectrum is difficult to obtain [4]. Anomaly detection does not require any a priori information of targets spectrum and can effectively mark the features of objects that differ from the background using only statistical identification methods. Therefore, it is widely used and has proven to be useful in a variety of applications.

In the well-known Reed-Xiaoli (RX) [5] method, the similarity between testing pixel and background pixels is calculated by typical Mahalanobis distance, and it is directly based on the assumption that hyperspectral background confirms to Gaussian normal distribution. When considering the entire image as a Gaussian background model, it is called global RX (GRX) [5]. If the RX detector estimates the background model using local statistics, it is called local RX (LRX) [6]. However, the distribution of background is extremely complicated and cannot be described using only a multivariate normal distribution. Therefore, some improved RX-based methods have been investigated. The weighted RX (WRX) and linear filter RX (LFRX) [7] aim at increasing the probability of anomalous pixels by improving estimation

* Corresponding author (email: liwei089@ieee.org)

of the background statistics. In addition, some nonlinear kernel-based methods have also achieved better anomaly detection performances; For example, the kernel RX [8] detection method effectively solves the spectral inseparability problem of linear space by using nonlinear kernel functions to map original space to high-dimensional feature space.

In recent years, linear representation, including sparse representation and linear representation, has been successfully applied to hyperspectral anomaly detection. In sparse representation, these methods aim to represent the entire image as concisely as possible with fewer atoms, such as sparse representation detector (SRD) [9], low-rank and sparse representation (LRASR) [10] and multiple local windows and the low-rank representation sum-to-one model (MLW_LRRSTO) [11]. In linear representation-based methods, collaborative representation detector (CRD) [12] has achieved satisfactory detection performance, which is directly based on the concept that a central pixel can be approximated by its spatial neighboring background pixels, but anomalies cannot. However, detection accuracy of these methods is heavily dependent on the quality of the dictionary construction. They only consider spectral information and do not fully utilize spatial information, making it difficult to achieve satisfactory results.

Recently, Li et al. [13] proposed a transferred deep convolutional neural network detector (CNND) to make full use of neighboring differences between pixel pairs. Tao et al. [14] presented a fractional Fourier entropy-based RX (FrFE-RX) detector, where fractional Fourier transform was employed as preprocessing to obtain features in an intermediate domain between the original reflectance spectrum and its Fourier transform. Furthermore, some background purification methods have recently received a lot of attention. Vafadar et al. [15] developed a collaborative representation-based with outlier removal anomaly detector (CRDBORAD), which obtained relatively pure background pixels by removing some suspected anomaly pixels. Subsequently, Su et al. [16] put forward CRD combined with principal component analysis (PCAroCRD). Considering the role of background estimation and suppression in anomaly detection, Zhang et al. [17] further designed a background purification-based framework. Zhao et al. [18] developed another nonparametric background refinement method based on the local density (BRMLD) to refine background information. To make full use of statistical information of local background, Tan et al. [19] also proposed a local summation unsupervised nearest regularized subspace with an outlier removal anomaly detector (LSUNRSORAD) to improve detection performance.

However, among these background purification-based methods, both background density calculation and local multi-window summation calculation are time-consuming. Therefore, considering positive correlation between coefficients and contribution of background pixels to a testing pixel in these linear representation methods, an effective solution for purifying background pixels using the representation coefficient is proposed. To obtain initial representation coefficients to purify background pixels, the least squares method is used. In addition, considering that targets first seen in the human visual system are often salient [20], anomalies should also be salient. Therefore, saliency weight of each pixel in an inner window is calculated to differentitate between anomalies and background. These considerations have inspired the development of a collaborative representation detector with background purification and saliency weight (CRDBPSW). To begin, the least squares method is used to calculate preliminary representation coefficients. Then, the mathematical statistics method is utilized to purify background pixels. Finally, a state-of-the-art CRD is used to obtain the final detection map. Meanwhile, saliency weight is imposed to improve the robustness of the proposed CRDBPSW.

The contributions of our proposed CRDBPSW method can be summarized as follows. (1) Different from other background purification methods, the least squares technique is used for the first time to refine the local background, where the contribution of the background pixels to the test pixel is determined according to the value of linear representation coefficients. (2) The saliency weight is introduced into the collaborative representation and the saliency weight value of the testing pixel is estimated for the first time by the local background pixels within the inner window, and is weighted into the linear representation process.

2 Proposed anomaly detection framework

During background modeling in traditional methods [12], heterogeneous pixels in the background may affect the accuracy of linear representation. Thus, it is necessary to purify background pixels. Therefore, an automatic outlier removal strategy based on initial coefficients to purify background pixels is designed. Considering that representation coefficients represent the contribution of neighboring pixels to the testing

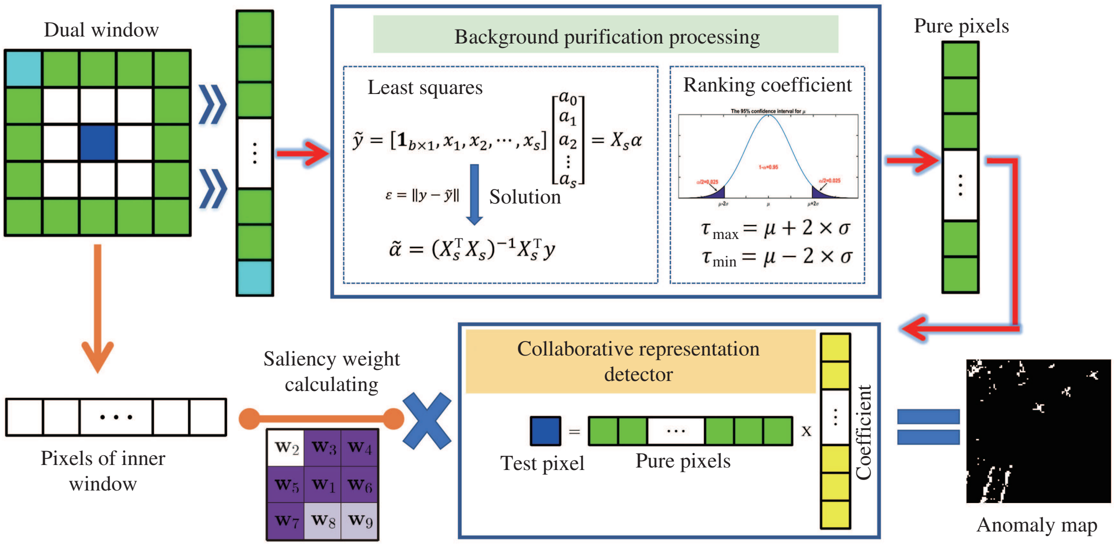

Figure 1 (Color online) Schematic of the proposed background purification framework.

pixel in linear representation methods, the classic least squares method is used to refine the background pixels. Figure 1 displays a flowchart of the proposed background purification framework, which consists of the following steps. To begin, background pixels in the dual window are purified using the least squares method. After that, the saliency weight of pixels in an inner window is computed. Finally, CRD is employed to linearly represent testing pixels by purified background. Simultaneously, the saliency weight is multiplied to represent the results for better separation.

2.1 Least squares-based background purification

For a given hyperspectral imagery dataset $\boldsymbol{X} \in \mathbb{R}^{b\times rc}$, b be number of spectral bands and r, c be the row and column, respectively. Based on the concept that a testing pixel can be linearly represented by its neighboring pixels, the testing pixel $\boldsymbol{y}$ with the size of $b\times 1$ can be approximated as

$$\tilde{\boldsymbol{y}} = a_0 + a_1\boldsymbol{x}_1 + a_2\boldsymbol{x}_2 + \cdots + a_s\boldsymbol{x}_s = \boldsymbol{X}_s \cdot \boldsymbol{\alpha}, \tag{1}$$

where $\tilde{\boldsymbol{y}}$ is an approximation vector of $\boldsymbol{y}$, $\boldsymbol{X}_s = [\mathbf{1}_{b\times1}, \boldsymbol{x}_1, \boldsymbol{x}_2, \ldots, \boldsymbol{x}_s]$ are the surrounding pixels between the outer and inner windows. $\mathbf{1}_{b\times1}$ is a column vector, whose all elements are 1. $\boldsymbol{\alpha} = [a_0, a_1, a_2, \ldots, a_s]^{\mathrm{T}}$ is the coefficient vector. s is the number of background pixels within dual window and can be calculated by

$$s = \omega_{\mathrm{out}} \times \omega_{\mathrm{out}} - \omega_{\mathrm{in}} \times \omega_{\mathrm{in}}, \tag{2}$$

where ω_{out} and ω_{in} are outer and inner window sizes, respectively. In order to minimize the linear prediction error $\varepsilon = \|\boldsymbol{y} - \tilde{\boldsymbol{y}}\|$, the least squares solution [21] is used, and vector $\boldsymbol{\alpha}$ can be estimated as

$$\tilde{\boldsymbol{\alpha}} = (X_s^{\mathrm{T}}X_s)^{-1}X_s^{\mathrm{T}}y. \tag{3}$$

After obtaining initial coefficients, these values in vector $\tilde{\boldsymbol{\alpha}}$ need to be sorted in descending order. Then, according to statistical analysis, m coefficients that contribute the most to the testing pixel are selected. In vector $\boldsymbol{\alpha}$, representation coefficient a_0 is a constant and does not represent any pixel, so it can be removed directly. Coefficient vector at this time becomes $[a_1, a_2, \ldots, a_s]$. After the coefficients are sorted from the largest to the smallest, it is represented,

$$[a_{\max1}, a_{\max2}, \ldots, a_{\max s}], \tag{4}$$

where $a_{\max1} > a_{\max2} > \cdots > a_{\max s}$, $a_{\max i} \in [a_1, a_2, \ldots, a_s]$. As shown in Figure 2, it is assumed that background imagery obeys a normal distribution and, when confidence interval is 95%, the value of α-quantile is 0.05, that is, $\alpha/2$ is equal to 0.025. The distribution table can then be used to calculate

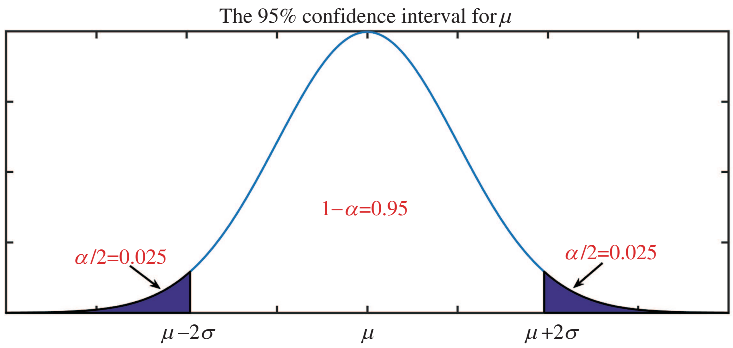

Figure 2 (Color online) Determination of maximum and minimum thresholds according to the confidence interval.

the maximum and minimum thresholds. This guarantees that the sample mean is within two standard deviations of the overall mean. Therefore, two formulas are obtained [15, 19] as follows:

$$\tau_{\max} = \mu + 2 \times \sigma, \tag{5}$$

$$\tau_{\min} = \mu - 2 \times \sigma, \tag{6}$$

where μ and σ are mean and standard deviation of these background pixels $\boldsymbol{X}_s$, and $\tau_{\max}$ and $\tau_{\min}$ represent maximum and minimum of these background pixels' intensities, respectively. It should be noted that, unlike a single band image, its intensity value is the digital value. However, because hyperspectral images contain a wealth of bands, the sum of the digital values of all bands is used to calculate the image's intensity value. The number of pixels between $\tau_{\max}$ and $\tau_{\min}$, denoted as m, is counted. Then, background pixels corresponding to m maximum coefficients are selected as the purified background,

$$\boldsymbol{X}_m = [\boldsymbol{x}_{\max 1}, \boldsymbol{x}_{\max 2}, \ldots, \boldsymbol{x}_{\max m}], \tag{7}$$

where $m < s$ and $\boldsymbol{X}_m$ represent the purified background pixels.

2.2 Collaborative representation detection with saliency weight

After obtaining purified background pixels, CRD is adopted to detect anomalous pixels. Different from the typical least squares method, in collaborative representation [12], objective function is to find weight vector $\boldsymbol{\varphi}$ under constraint that $\|\boldsymbol{\varphi}\|_2^2$ by minimizing $\|\boldsymbol{y} - \boldsymbol{X}_r\boldsymbol{\varphi}\|_2^2$. Therefore, the new objective function is

$$\operatorname{argmin}_{\varphi}\|\boldsymbol{y} - \boldsymbol{X_r}\boldsymbol{\varphi}\|_2^2 + \lambda\|\boldsymbol{\varphi}\|_2^2, \tag{8}$$

where $\boldsymbol{X}_r$ represents the purified background, such as $\boldsymbol{X}_m$, $\boldsymbol{\varphi} = [b_1, b_2, \ldots, b_r]^{\mathrm{T}}$ is a weight vector, and λ is Lagrange multiplier. For those background pixels that are quite different from the testing pixel, coefficients should be small, and the penalty for having a large coefficient must be heavy. Therefore, a distance-weighted Tikhonov regularization is considered to adjust the weight vector

$$\boldsymbol{\Gamma}_y = \begin{bmatrix} \|\boldsymbol{y} - \boldsymbol{x}_1\|_2 & \ldots & 0 \\ \vdots & \ddots & \vdots \\ 0 & \ldots & \|\boldsymbol{y} - \boldsymbol{x}_r\|_2 \end{bmatrix}. \tag{9}$$

The objective function after adding the Tikhonov regularization can be converted to

$$\operatorname{argmin}_{\varphi}\|\boldsymbol{y} - \boldsymbol{X}_r\varphi\|_2^2 + \lambda\|\boldsymbol{\Gamma}_y\boldsymbol{\varphi}\|_2^2. \tag{10}$$

Using the Lagrange multiplier method, a final solution can be obtained,

$$\tilde{\boldsymbol{\varphi}} = (\boldsymbol{X}_r^{\mathrm{T}}\boldsymbol{X}_r + \lambda\boldsymbol{\Gamma}_y^{\mathrm{T}}\boldsymbol{\Gamma}_y)^{-1}\boldsymbol{X}_r^{\mathrm{T}}\boldsymbol{y}. \tag{11}$$

Generally, the closer the spatial distance between two pixels is, the higher the spectral similarity is. However, to the best of our knowledge, pixels contained in an inner window are rarely used in many methods based on dual-window, and the influence of adjacent pixels on the testing pixel is not considered. Targets seen for the first time are generally regarded as significant in the human visual system. Similarly, anomalous targets should be significant in comparison to the background. Therefore, to address this issue, saliency weight is used to distinguish between anomalous targets and background. When the spectral information of a testing pixel is clearly different from that of its neighboring pixels, the pixel is said to be regional saliency. In this work, spectral angular distance between local pixels in inner window and testing pixel is used to define a saliency weight [20, 22],

$$d_{\text{saliency}}(\boldsymbol{x}_i, \boldsymbol{y}) = \frac{d_{\text{spectral}}(\boldsymbol{x}_i, \boldsymbol{y})}{1 + c d_{\text{position}}(\boldsymbol{x}_i, \boldsymbol{y})}, \tag{12}$$

where $\boldsymbol{x}_i$ is surrounding pixels contained in an inner window, c is a constant, which has little effect on the final result. Here its value is set to 1. $d_{\text{spectral}}(\cdot)$ and $d_{\text{position}}(\cdot)$ are spectral angular distance and Euclidean distance between position coordinates,

$$d_{\text{spectral}}(\boldsymbol{x}_i, \boldsymbol{y}) = \arccos\left(\frac{\sum_{i=1}^{N} \boldsymbol{x}_i \boldsymbol{y}}{\sqrt{\sum_{i=1}^{N} \boldsymbol{x}_i \sum_{i=1}^{N} \boldsymbol{y}}}\right), \tag{13}$$

where $N = \omega_{\text{in}} \times \omega_{\text{in}} - 1$ is the number of background pixels in an inner window. The position coordinates of $\boldsymbol{y}$ and $\boldsymbol{x}_i$ are denoted as (i, j) and (k, l), respectively. Then, d_{position} can be expressed by

$$d_{\text{position}}(\boldsymbol{x}_i, \boldsymbol{y}) = \sqrt{(i-k)^2 + (j-l)^2}. \tag{14}$$

Finally, we take the average of all weight as the saliency weight of the testing pixel,

$$d_{\text{saliency\_eva}} = \frac{\sum_{i=1}^{N} d_{\text{saliency}}}{N}. \tag{15}$$

Through a sliding window, the saliency weight of a testing pixel in each window is calculated, which constitutes a saliency map. A final probability map of anomaly detection can be obtained,

$$D(x) = \|\boldsymbol{y} - \boldsymbol{X}_r \tilde{\varphi}\|_2 \cdot d_{\text{saliency\_eva}}. \tag{16}$$

The overall description of the proposed CRDBPSW is briefly described in Algorithm 1.

Algorithm 1 Proposed CRDBPSW for hyperspectral anomaly detection

Input: Three-dimensional hyperspectral imagery, window size (ω_{out}, ω_{in}) and parameter λ;
Output: Anomaly detection map $D(\boldsymbol{x})$;
1: Reshaping three-dimensional hyperspectral cube to two-dimensional data;
2: **For all** pixels **do**
3: Calculating the preliminary coefficient vector $\tilde{\boldsymbol{\alpha}}$ of each test pixel by (3);
4: Calculating the threshold by (5) and (6) and getting the purification background $\boldsymbol{X}_m$ by (7);
5: Let $\boldsymbol{X}_r = \boldsymbol{X}_m$, and then calculate the weight vector $\tilde{\boldsymbol{\varphi}}$ by a closed-form of (11);
6: Calculating the saliency weight of test pixel by (15);
7: Calculating the final detection result by (16);
8: **End for**

2.3 Analysis on proposed CRDBPSW

In the proposed CRDBPSW, background purification processing is attempted to reduce the influence of heterogeneous pixels in the background during linear representation, thereby achieving better approximation. To illustrate the benefits, Figure 3 shows residual values of CRD and the proposed CRDBPSW using background pixels in the San Diego dataset (will be introduced in Subsection 3.1). CRD means that all pixels within the inner and outer windows are used for linear representation, whereas CRDBPSW means that only pixels that have been preserved after background purification are used. It is clear that the black curve representing CRDBPSW is generally lower than the blue curve representing CRD, indicating that CRDBPSW's approximatio is more accurate than CRD's. It further confirms that the proposed CRDBPSW can significantly remove heterogeneous pixels in the background.

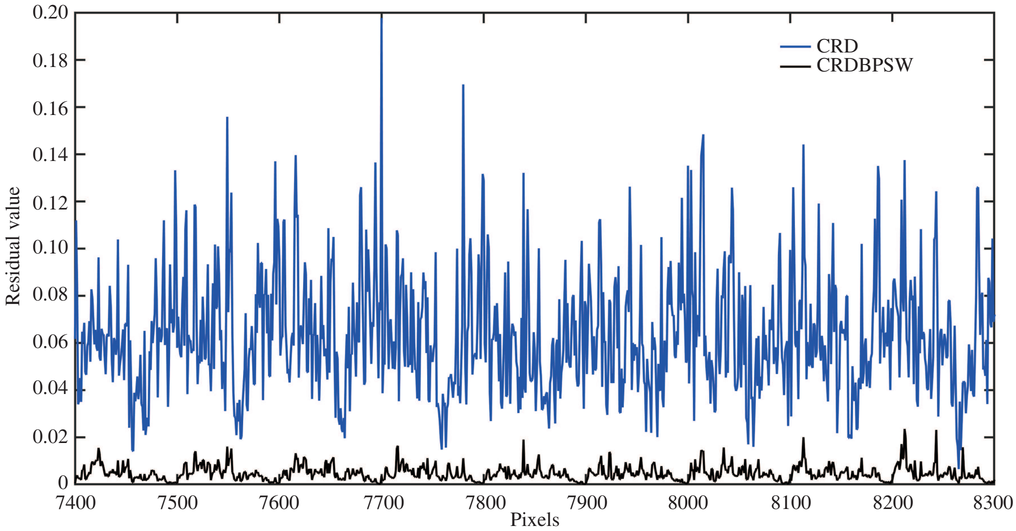

Figure 3 (Color online) Residual values of CRD and the proposed CRDBPSW using background pixels in the San Diego dataset.

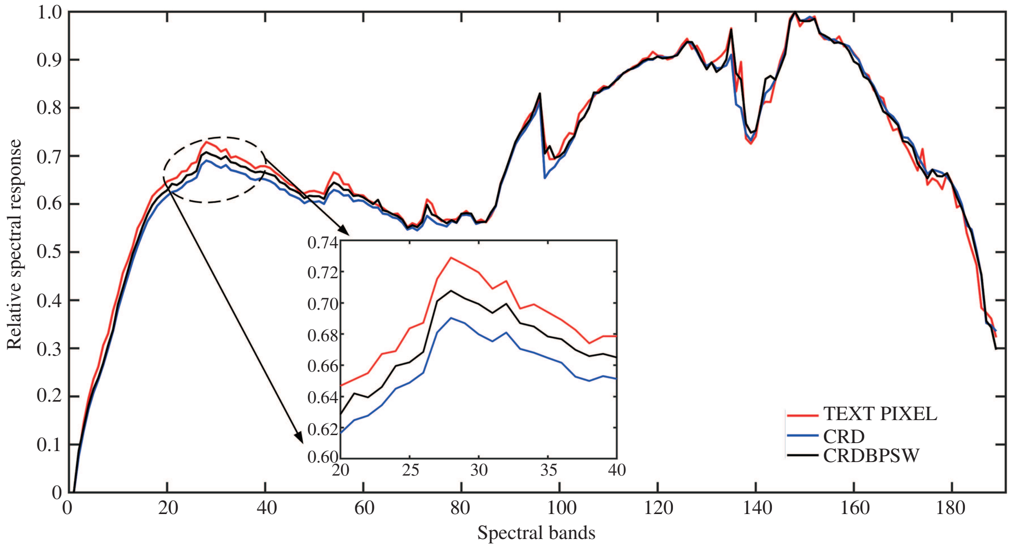

Figure 4 (Color online) Comparison of spectral signatures using one chosen background pixel.

Figure 4 illustrates the comparison of spectral signatures using one chosen background pixel, where red, blue, and black curves represent the original spectral signature, approximation using CRD, and the one using CRDBPSW, respectively. The trend of the black and blue curves is consistent with the trend of the red curve, indicating that the original background spectral information of the chosen testing pixel can be effectively represented by the linear representation using background pixels. The slight difference between the blue curve and black one can be observed when the abscissa of the spectral curve is in the range of 1–80, 130–140, and 165–189, and the trend of the black curve is closer to the red one, which reflects that the proposed CRDBPSW can restore spectral signatures in HSI.

3 Experiments and discussion

3.1 Datasets description

The first image was obtained by an airborne visible/infrared imaging spectrometer (AVIRIS) sensor flying in the Gulfport area. The flight time is July 7, 2010. The image is made up of 100×100 pixels with a spatial resolution of 3.4 m. After removing the corresponding bands, it has 191 spectral bands; the anomalies are caused by airplanes. The scene and the ground-truth map are shown in Figure 5. The

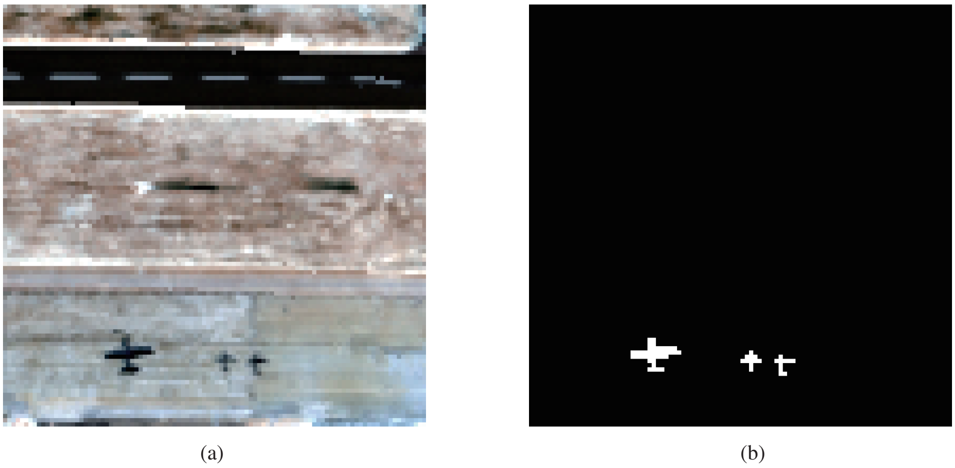

Figure 5 (Color online) Illustration of the Gulfport dataset. (a) Pseudo color (RGB: 80, 60, 50); (b) the ground-truth map.

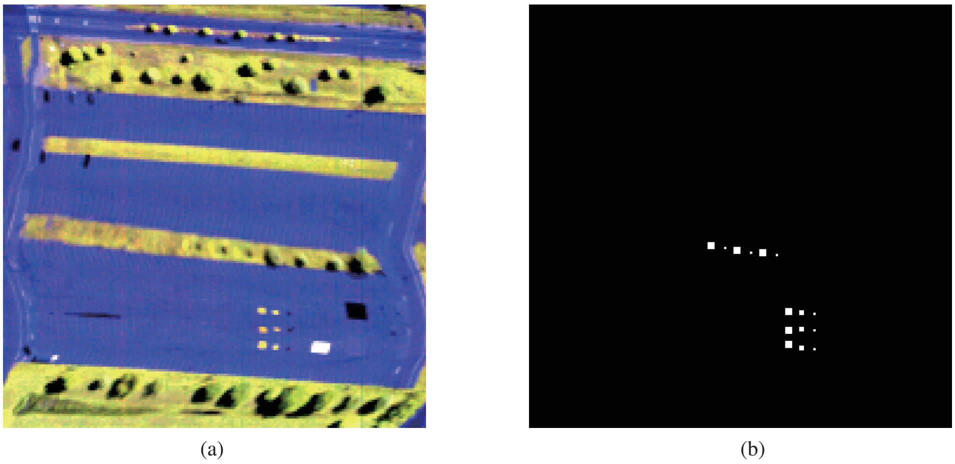

Figure 6 (Color online) Illustration of the SpecTIR dataset. (a) Pseudo color (RGB: 53, 34, 14); (b) the ground-truth map.

reference map of the sample image is manually labeled with the help of the environment for visualizing images (ENVI) software. The dataset has been made available on the first author's homepage [4].

The second image was obtained by the SpecTIR hyperspectral airborne Rochester experiment [14, 23] with a spatial resolution of 1 m. This image is of size $180 \times 180 \times 120$, in which the noisy bands have been removed. Anomalies consist of man-made colorful square fabrics. The image and the ground-truth of anomalies are illustrated in Figure 6.

The third image is a part of the San Diego airport in the USA, which was acquired by the AVIRIS sensor with a spatial resolution of 3.5 m. After removing the corresponding noisy bands, this image is of size $100 \times 100 \times 189$, which is the top-left part of the whole scene. Anomalies consist of airplanes containing fifty-eight pixels [24]. The sub-image and the ground-truth map are illustrated in Figure 7.

3.2 Parameter analysis

The initial choices of different parameters are important for the proposed CRDBPSW, which involve three parameters: λ, ω_{out} and ω_{in}. For CRD, its performance is insensitive to parameter λ and window size. Same as CRD, the detection performance of the proposed CRDBPSW is also insensitive to regularization parameter λ and window size. Therefore, by fixing λ as 10^{-6} as suggested in [4, 12], and varying ω_{in} from 3 to 15 and ω_{out} from 5 to 19, the detection performance of CRDBPSW under different parameters is collected.

Similarly, for LRX, by using the same way to change ω_{in} from 3 to 15 and ω_{out} from 5 to 19, detection performance under different window sizes is collected. It should be emphasized that in the following comparative experiments, detection results of LRX, robust principal component analysis (RPCA), and CRD are all optimal. As shown in Figures 8–10, detection performances of different datasets are provided.

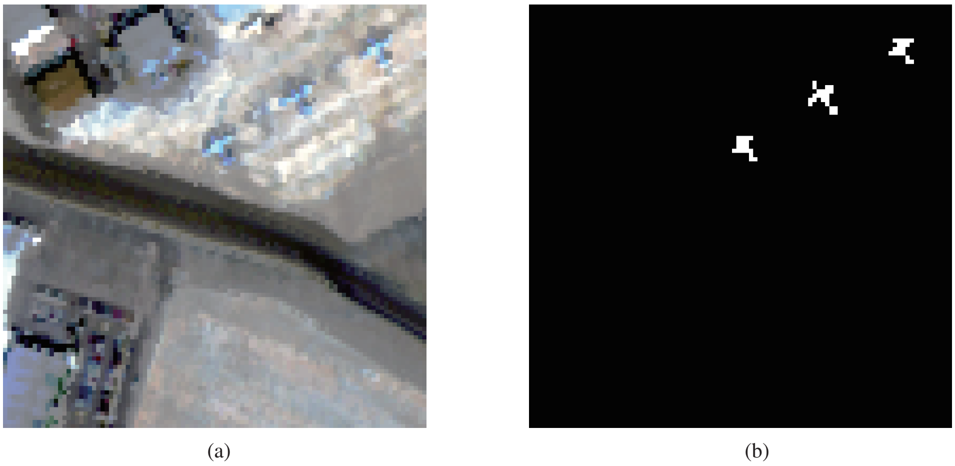

Figure 7 (Color online) Illustration of the San Diego dataset. (a) Pseudo color (RGB: 22, 13, 4); (b) the ground-truth map.

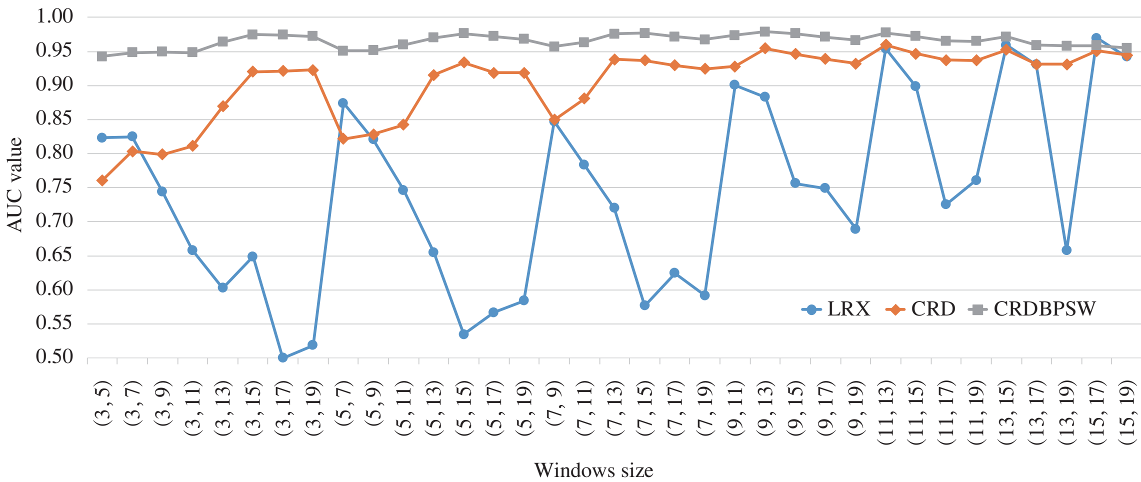

Figure 8 (Color online) AUC values of different windows sizes in the Gulfport dataset.

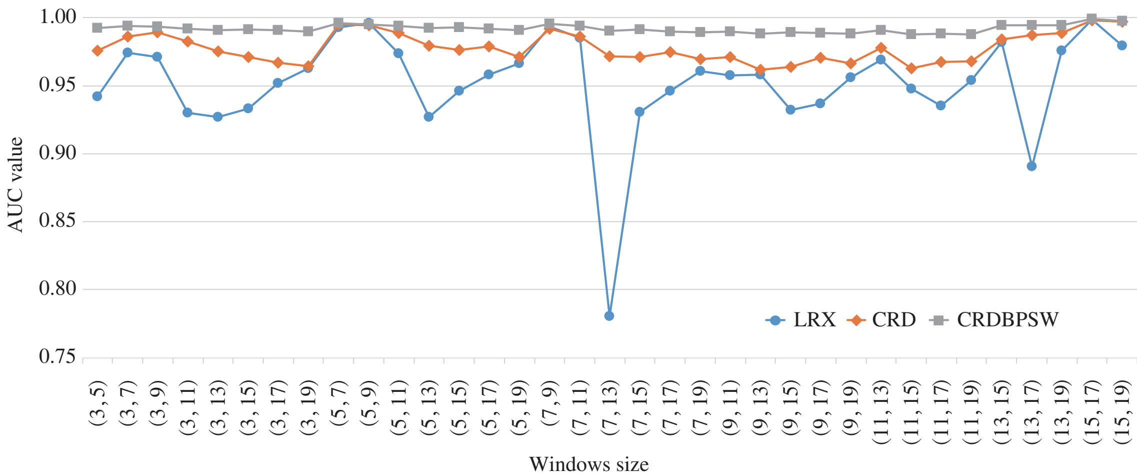

Figure 9 (Color online) AUC values of different windows sizes in the SpecTIR dataset.

It can be seen in Figure 8 that for LRX and CRD, performance curves change greatly with various window sizes, especially when the size of inner and outer windows differs greatly and detector performance is poor.

For CRDBPSW, detection performance is relatively stable, which shows that the proposed method reflects better robustness. In Figure 9, a similar conclusion can be drawn that the stability and average

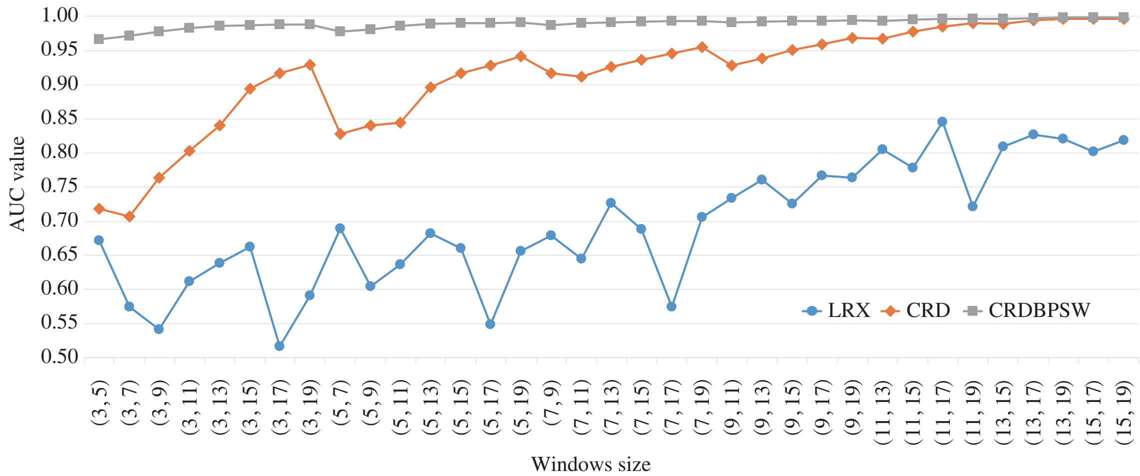

Figure 10 (Color online) AUC values of different windows sizes in the San Diego dataset.

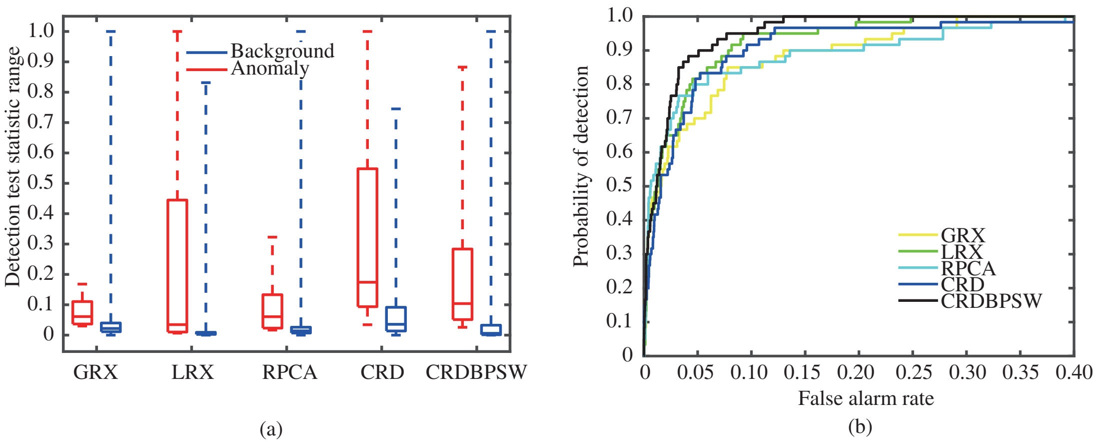

Figure 11 (Color online) Detection performance using the Gulfport dataset. (a) Statistical separability analysis; (b) ROC curves.

performance of the proposed CRDBPSW using the SpecTIR dataset is superior to LRX and CRD. Similarly, it can be seen using the San Diego dataset as shown in Figure 10 that the proposed CRDBPSW can still maintain good stability when window size varies, and average detection performance is also better than LRX and CRD.

3.3 Detection performance

The anomaly detection performance of the proposed method is compared with some other detectors. Four commonly used anomaly detectors, such as the GRX, LRX, RPCA, and CRD, are used in the experiments. For qualitative and quantitative comparison, statistical separability analysis [19], receiver operating characteristic (ROC), and area under the curve (AUC) [25] metric are utilized as main criteria for evaluation.

For the Gulfport dataset, separability between anomalous targets and background, and output value range of different detection methods are displayed in Figure 11(a). The red box denotes the range of anomalous targets, while the blue box denotes the range of background. The separation between anomalous targets and background is represented by the interval between the red and blue boxes. The height of the box represents the degree to which these methods suppress anomaly and background. In general, the lower the blue box height, the stronger the background suppression, which aids in the separation of background and anomaly. As shown in Figure 11(a), the interval between the red and blue boxes of the proposed CRDBPSW method is larger than GRX, LRX, RPCA, and CRD methods, which indicates that the proposed CRDBPSW method can separate anomalous targets from the background more effectively. The blue box height of the LRX method is the lowest, which indicates that the LRX

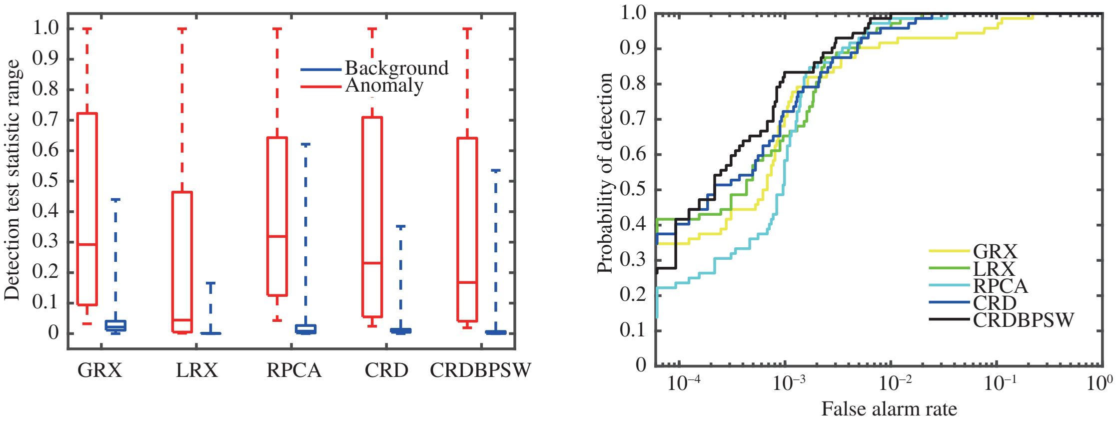

(a) (b)

Figure 12 (Color online) Detection performance using the SpecTIR dataset. (a) Statistical separability analysis; (b) ROC curves.

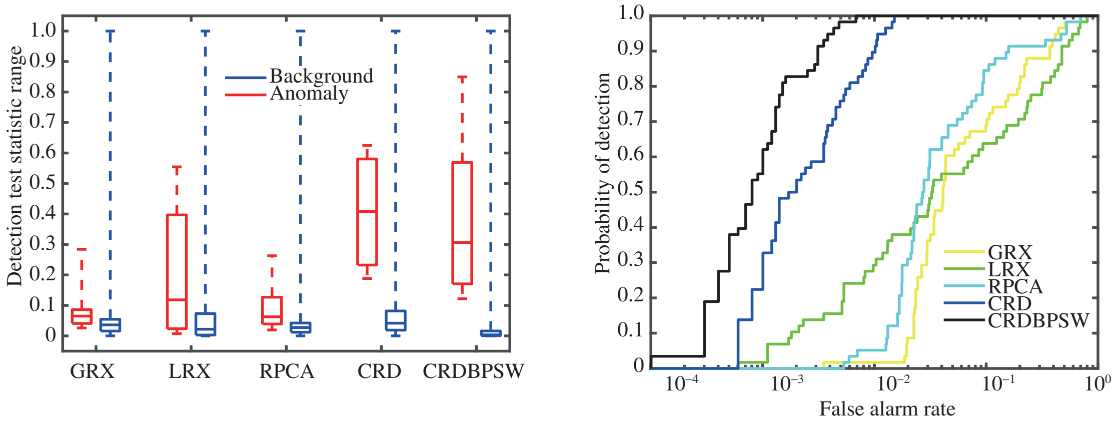

(a) (b)

Figure 13 (Color online) Detection performance using the San Diego dataset. (a) Statistical separability analysis; (b) ROC curves.

method has the best background suppression compared with other methods. However, the separation of LRX from anomalous targets and background is poor.

For the SpecTIR dataset, as shown in Figure 12(a), the blue boxes representing LRX, CRD, and CRDBPSW are lower than those boxes representing GRX and RPCA, which indicates that LRX, CRD, and CRDBPSW methods have better background suppression compared with other methods. The interval between red and blue boxes representing CRDBPSW and CRD is larger than the interval between red and blue boxes representing LRX, indicating that CRDBPSW and CRD methods can more effectively separate background and anomalous targets than LRX. Furthermore, the the proposed CRDBPSW has slightly better background suppression than CRD. Similarly, the same conclusion can be drawn from the San Diego dataset as shown in Figure 13(a), where it is more intuitively that the proposed CRDBPSW can effectively suppress background and separate anomalous targets when compared with other methods.

To compare the detection performance of various methods more intuitively, ROC curves are provided. As shown in Figure 11(b), in the Gulfport dataset, it is easy to find that compared with other detection methods, the black ROC curve representing the proposed CRDBPSW is obviously on the top left, which reflects that the performance of CRDBPSW is better than other methods. For the SpecTIR dataset, as shown in Figure 12(b), compared with other detection methods, the curve of CRDBPSW is obviously on the top left, which confirms that the effectiveness of the proposed CRDBPSW. Similarly, for the San Diego dataset, the same conclusion can be drawn that the ROC curve of the proposed CRDBPSW is closest to the upper left corner in Figure 13(b), which also means that the detection performance of the proposed method is better than other methods.

For quantitative comparison, AUC values are used as the main criteria to evaluate the detection performance, as listed in Table 1. The detection results of CRDBPSW are better than other methods for

Table 1 AUC values of different anomaly detectors using three experimental datasets

Method	GRX	LRX	RPCA	CRD	CRDBPSW
Gulfport	0.95260	0.96940	0.95348	0.95992	0.97913
SpecTIR	0.99138	0.99846	0.99827	0.99830	0.99909
San Diego	0.88854	0.84557	0.91896	0.99635	0.99873

Table 2 Execution time of different anomaly detectors using three experimental datasets (unit: s)

Method	GRX	LRX	RPCA	CRD	CRDBPSW
Gulfport	0.28	36.22	2.71	4.33	15.49
SpecTIR	0.22	39.86	3.86	15.13	37.73
San Diego	0.10	47.93	2.32	14.51	29.42

these three experimental datasets, especially for the Gulfport dataset; compared with the CRD method, the improvement of CRDBPSW is approximately 2%. Table 2 provides the computational cost of various detection methods. Although the proposed CRDBPSW takes less time to execute than LRX when compared to other traditional detection methods, the calculation cost is still high, particularly for the SpecTIR dataset. The reason for this is that additional background purification and saliency weight calculations have been implemented.

4 Conclusion

In this paper, a background purification framework for hyperspectral anomaly detection was proposed. The classic least squares method was first used in the proposed CRDBPSW framework to purify background in HSI. Simultaneously, saliency analysis was designed to further improve detection performance by calculating saliency weight between adjacent pixels and the testing pixel to make full use of spatial information between adjacent pixels in an inner window. Experiments with three real hyperspectral datasets confirmed that the proposed method was stable to different window size changes and that its detection performance always outperformed some traditional anomaly detection methods.

Acknowledgements This work was supported by National Key Research and Development Project of China (Grant No. 017YFB-0503903), National Natural Science Foundation of China (Grant Nos. 61922013, 61421001, U1833203), Key Scientific and Technological Projects in Henan Province (Grant No. 192102210106), and Beijing Natural Science Foundation (Grant No. L191004).

References

1 Li Y F, Li J, He L, et al. A new sensor bias-driven spatio-temporal fusion model based on convolutional neural networks. Sci China Inf Sci, 2020, 63: 140302
2 He N J, Fang L Y, Plaza A. Hybrid first and second order attention Unet for building segmentation in remote sensing images. Sci China Inf Sci, 2020, 63: 140305
3 Liu X B, Qiao Y L, Xiong Y H, et al. Cascade conditional generative adversarial nets for spatial-spectral hyperspectral sample generation. Sci China Inf Sci, 2020, 63: 140306
4 Kang X D, Zhang X P, Li S T, et al. Hyperspectral anomaly detection with attribute and edge-preserving filters. IEEE Trans Geosci Remote Sens, 2017, 55: 5600–5611
5 Reed I S, Yu X L. Adaptive multiple-band CFAR detection of an optical pattern with unknown spectral distribution. IEEE Trans Acoust Speech Signal Process, 1990, 38: 1760–1770
6 Matteoli S, Diani M, Corsini G. Improved estimation of local background covariance matrix for anomaly detection in hyperspectral images. Opt Eng, 2010, 49, 046201
7 Guo Q D, Zhang B, Ran Q, et al. Weighted-RXD and linear filter-based RXD: improving background statistics estimation for anomaly detection in hyperspectral imagery. IEEE J Sel Top Appl Earth Observations Remote Sens, 2014, 7: 2351–2366
8 Kwon H, Nasrabadi N M. Kernel RX-algorithm: a nonlinear anomaly detector for hyperspectral imagery. IEEE Trans Geosci Remote Sens, 2005, 43: 388–397
9 Chen Y, Nasrabadi N M, Tran T D. Simultaneous joint sparsity model for target detection in hyperspectral imagery. IEEE Geosci Remote Sens Lett, 2011, 8: 676–680
10 Xu Y, Wu Z B, Li J, et al. Anomaly detection in hyperspectral images based on low-rank and sparse representation. IEEE Trans Geosci Remote Sens, 2016, 54: 1990–2000
11 Tan K, Hou Z F, Ma D L, et al. Anomaly detection in hyperspectral imagery based on low-rank representation incorporating a spatial constraint. Remote Sens, 2019, 11: 1578
12 Li W, Du Q. Collaborative representation for hyperspectral anomaly detection. IEEE Trans Geosci Remote Sens, 2015, 53: 1463–1474
13 Li W, Wu G D, Du Q. Transferred deep learning for anomaly detection in hyperspectral imagery. IEEE Geosci Remote Sens Lett, 2017, 14: 597–601
14 Tao R, Zhao X D, Li W, et al. Hyperspectral anomaly detection by fractional fourier entropy. IEEE J Sel Top Appl Earth Observations Remote Sens, 2019, 12: 4920–4929
15 Vafadar M, Ghassemian H. Hyperspectral anomaly detection using outlier removal from collaborative representation. In: Proceedings of the 3rd International Conference on Pattern Recognition and Image Analysis (IPRIA), Shahrekord, 2017. 13–19

16 Su H J, Wu Z Y, Du Q, et al. Hyperspectral anomaly detection using collaborative representation with outlier removal. IEEE J Sel Top Appl Earth Observations Remote Sens, 2018, 11: 5029–5038
17 Zhang Y, Fan Y G, Xu M M. A background-purification-based framework for anomaly target detection in hyperspectral imagery. IEEE Geosci Remote Sens Lett, 2020, 17: 1238–1242
18 Zhao C H, Wang X P, Yao X F, et al. A background refinement method based on local density for hyperspectral anomaly detection. J Cent South Univ, 2018, 25: 84–94
19 Tan K, Hou Z F, Wu F Y, et al. Anomaly detection for hyperspectral imagery based on the regularized subspace method and collaborative representation. Remote Sens, 2019, 11: 1318
20 Goferman S, Zelnik-Manor L, Tal A. Context-aware saliency detection. IEEE Trans Pattern Anal Mach Intell, 2012, 34: 1915–1926
21 Tan K, Li E Z, Du Q, et al. Hyperspectral image classification using band selection and morphological profiles. IEEE J Sel Top Appl Earth Observations Remote Sens, 2014, 7: 40–48
22 Liu W H, Feng X P, Wang S, et al. Random selection-based adaptive saliency-weighted RXD anomaly detection for hyperspectral imagery. Int J Remote Sens, 2018, 39: 2139–2158
23 Herweg J A, Kerekes J P, Weatherbee O, et al. Spectir hyperspectral airborne rochester experiment data collection campaign. In: Proceedings of SPIE, 2012. 839028
24 Zhao R, Du B, Zhang L P. Hyperspectral anomaly detection via a sparsity score estimation framework. IEEE Trans Geosci Remote Sens, 2017, 55: 3208–3222
25 Hanley J A, McNeil B J. The meaning and use of the area under a receiver operating characteristic (ROC) curve. Radiology, 1982, 143: 29–36